was compared for the electrochemical oxidation of uncomplexed (*S*,*S*)- and (*R*,*R*)-tartrate. CuO has been shown by other workers to be a potent electrocatalyst for the oxidation of carbohydrates, amino acids, simple alcohols, aliphatic diols, and alkyl polyethoxy alcohol detergents[30]. Chiral recognition by CuO has not, to our knowledge, been demonstrated previously. Linear sweep voltammograms are shown in Fig. 4 for the oxidation of (*S*,*S*)- and (*R*,*R*)-tartrate on CuO electrodes that were deposited from Cu(II)(*S*,*S*)-tartrate (Fig. 4a) and Cu(II)(*R*,*R*)-tartrate (Fig. 4b). The (*S*)-CuO film grown in (*S*,*S*)-tartrate is more active for the oxidation of the (*S*,*S*)-tartrate, and the (*R*)-CuO film grown in (*R*,*R*)-tartrate is more active for the oxidation of the (*R*,*R*)-tartrate. A control film shown in Fig. 4c (which was deposited from a racemic mixture of the (*S*,*S*)- and (*R*,*R*)-tartrates) shows no selectivity for the oxidation of the enantiomers.

We believe that our approach should be quite general for the deposition of other enantiospecific catalysts, because it does not require that the materials crystallize in a chiral space group. One attractive potential application of such catalysts would be their use as post-chromatographic chiral electrochemical sensors, which would no longer require chiral separation before chemical detection. □

Methods

Solutions, sample preparation, and electrochemistry

The CuO films were deposited to a thickness of approximately 300 nm at 30 °C onto a polished and H_2-flame-annealed Au(001) single crystal at an anodic current density of $1\,\mathrm{mA\,cm^{-2}}$ from a solution of 0.2 M Cu(II), 0.2 M tartrate ion, and 3 M NaOH. Chiral recognition was demonstrated using uncomplexed tartrate ion as the target molecule. The linear sweep voltammograms in Fig. 4 were run at room temperature in unstirred solutions of 5 mM (*S*,*S*)- and (*R*,*R*)-tartrate in 0.1 M NaOH at a sweep rate of $10\,\mathrm{mV\,s^{-1}}$.

X-ray diffraction

X-ray diffraction measurements were done on a high-resolution Philips X'Pert MRD diffractometer. For the Bragg-Brentano scan, the primary optics module was a combination Göbel mirror and a two-crystal Ge(220) two-bounce hybrid monochromator, and the secondary optics module was a 0.18° parallel plate collimator. The hybrid monochromator produces pure CuKα_1 radiation ($\lambda = 0.1540562\,\mathrm{nm}$) with a divergence of 25 arcsec. Pole figures were obtained in point-focus mode using a crossed-slit collimator as the primary optics, and a 0.27° parallel plate collimator and flat graphite monochromator as the secondary optics. A 2θ value of 38.742° was used to probe the (111) reflection of CuO. Enantiomeric excesses were determined from CuO(111) azimuthal scans at $2\theta = 38.742°$ and $\chi = 63°$ by integrating the area under the (111) and ($\bar{1}\bar{1}\bar{1}$) peaks due to the R and S forms of CuO, respectively.

1. Stinson, S. C. Chiral pharmaceuticals. *Chem. Eng. News* **79**, 79–97 (2001).
2. Lorenzo, M. O., Baddeley, C. J., Muryn, C. & Raval, R. Extended surface chirality from supramolecular assemblies of adsorbed chiral molecules. *Nature* **404**, 376–379 (2000).
3. Humblot, V., Haq, S., Muryn, C., Hofer, W. A. & Raval, R. From local adsorption stresses to chiral surfaces: (R,R)-tartaric acid on Ni(110). *J. Am. Chem. Soc.* **124**, 503–510 (2002).
4. Kühnle, A., Linderoth, T. R., Hammer, B. & Besenbacher, F. Chiral recognition in dimerization of adsorbed cysteine observed by scanning tunnelling microscopy. *Nature* **415**, 891–893 (2002).
5. Izumi, Y. in *Advances in Catalysis* Vol. 32, 215–271 (Academic, New York, 1983).
6. LeBlond, C., Wang, J., Liu, J., Andrews, A. T. & Sun, Y.-K. Highly enantioselective heterogeneously catalyzed hydrogenation of α-ketoesters under mild conditions. *J. Am. Chem. Soc.* **121**, 4920–4921 (1999).
7. McFadden, C. F., Cremer, P. S. & Gellman, A. J. Adsorption of chiral alcohols on "chiral" metal surfaces. *Langmuir* **12**, 2483–2487 (1996).
8. Horvath, J. D. & Gellman, A. J. Enantiospecific desorption of R- and S-propylene oxide from a chiral Cu(643) surface. *J. Am. Chem. Soc.* **123**, 7953–7954 (2001).
9. Horvath, J. D. & Gellman, A. J. Enantiospecific desorption of chiral compounds from chiral Cu(643) and achiral Cu(111) surfaces. *J. Am. Chem. Soc.* **124**, 2384–2392 (2002).
10. Ahmadi, A., Attard, G., Feliu, J. & Rodes, A. Surface reactivity at "chiral" platinum surfaces. *Langmuir* **15**, 2420–2424 (1999).
11. Attard, G. A. *et al.* Temperature effects in the enantiomeric electro-oxidation of D- and L-glucose on Pt{643}S. *J. Phys. Chem. B* **103**, 1381–1385 (1999).
12. Attard, G. A. Electrochemical studies of enantioselectivity of chiral metal surfaces. *J. Phys. Chem. B* **105**, 3158–3167 (2001).
13. Sholl, D. S., Asthagiri, A. & Power, T. D. Naturally chiral metal surfaces as enantiospecific adsorbents. *J. Phys. Chem. B* **105**, 4771–4782 (2001).
14. Orme, C. A. *et al.* Formation of chiral morphologies through selective binding of amino acids to calcite surface steps. *Nature* **411**, 775–779 (2001).
15. Addadi, L. & Weiner, S. Crystals, asymmetry and life. *Nature* **411**, 753–755 (2001).
16. Teng, H. H., Dove, P. M., Orme, C. A. & De Yoreo, J. J. Thermodynamics of calcite growth: baseline for understanding biomineral formation. *Science* **282**, 724–727 (1998).
17. Cody, A. M. & Cody, R. D. Chiral habit modifications of gypsum from epitaxial-like adsorption of stereospecific growth inhibitors. *J. Cryst. Growth* **113**, 508–519 (1991).
18. Paunovic, M. & Schlesinger, M. *Fundamentals of Electrochemical Deposition* 167–186 (Wiley-Interscience, New York, 1998).
19. Josell, D., Wheeler, D., Huber, W. H. & Moffat, T. P. Superconformal electrodeposition in submicron features. *Phys. Rev. Lett.* **87**, 016102 (2001).
20. Vazhev, V. V. & Mardashev, Yu. S. A "memory" effect in formic and oxalic acid oxidation at gold electrodes. *Sov. Electrochem.* **16**, 1445–1447 (1980).
21. Switzer, J. A., Shumsky, M. G. & Bohannan, E. W. Electrodeposited ceramic single crystals. *Science* **284**, 293–296 (1999).
22. Bohannan, E. W., Shumsky, M. G. & Switzer, J. A. Epitaxial electrodeposition of copper(I) oxide on single-crystal Au(100). *Chem. Mater.* **11**, 2289–2291 (1999).
23. Sorenson, T. A., Morton, S. A., Waddill, G. D. & Switzer, J. A. Epitaxial electrodeposition of Fe₃O₄ thin films on the low-index planes of gold. *J. Am. Chem. Soc.* **124**, 7604–7609 (2002).
24. Switzer, J. A., Kothari, H. M. & Bohannan, E. W. Thermodynamic to kinetic transition in epitaxial electrodeposition. *J. Phys. Chem. B* **106**, 4027–4031 (2002).
25. Switzer, J. A., Liu, R., Bohannan, E. W. & Ernst, F. Epitaxial electrodeposition of a crystalline metal oxide onto single-crystalline silicon. *J. Phys. Chem. B* **106**, 12369–12372 (2002).
26. Poizot, P., Hung, C.-J., Nikiforov, M. P., Bohannan, E. W. & Switzer, J. A. An electrochemical method for CuO thin film deposition from aqueous solution. *Electrochem. Solid-State Lett.* **6**, C21–C25 (2003).
27. Catana, A., Locquet, J.-P., Paik, S. M. & Schuller, I. K. Local epitaxial growth of copper monoxide films on magnesium oxide. *Phys. Rev. B* **46**, 15477–15483 (1992).
28. Missavage, R. J., Belford, R. L. & Paul, I. C. Crystal and molecular structure of tetrasodium dicopper(II)-dl-tartrate decahydrate. *J. Coord. Chem.* **2**, 145–157 (1972).
29. Hazen, R. M., Filley, T. R. & Goodfriend, G. A. Selective adsorption of L- and D-amino acids on calcite: Implications for biochemical homochirality. *Proc. Natl Acad. Sci. USA* **98**, 5487–5490 (2001).
30. Xie, Y. & Huber, C. O. Electrocatalysis and amperometric detection using an electrode made of copper oxide and carbon paste. *Anal. Chem.* **63**, 1714–1719 (1991).

Episodic sediment accumulation on Amazonian flood plains influenced by El Niño/Southern Oscillation

Rolf Aalto[1,2], **Laurence Maurice-Bourgoin**[3], **Thomas Dunne**[4], **David R. Montgomery**[1,2], **Charles A. Nittrouer**[2] & **Jean-Loup Guyot**[5]

[1]*Quaternary Research Center and* [2]*Department of Earth and Space Sciences, University of Washington, Seattle, Washington 98195, USA*
[3]*Institut de Recherche pour le Développement, UMR Laboratoire des Mécanismes de Transfert en Géologie, CP 7091 Lago Sul, CEP 71619-970, Brasilia, DF, Brazil*
[4]*Donald Bren School of Environmental Science and Management and Department of Geological Sciences, University of California, Santa Barbara, California 93106, USA*
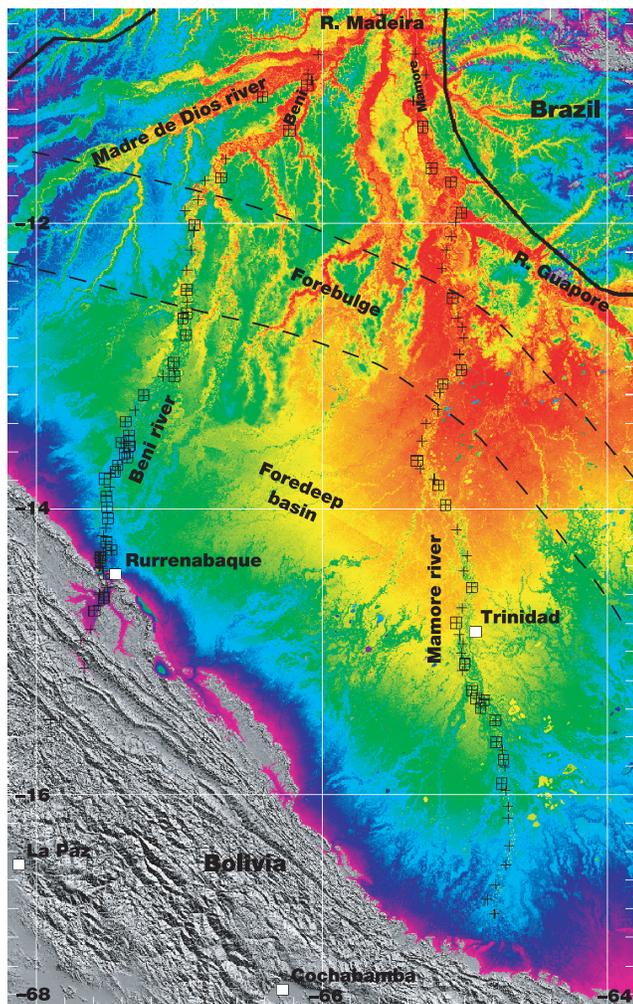[5]*IRD, UMR LMTG, CNRS/IRD Paul Sabatier University, F-31400 Toulouse, France*

....

Continental-scale rivers with a sandy bed sequester a significant proportion of their sediment load in flood plains. The spatial extent and depths of such deposits have been described[1,2], and flood-plain accumulation has been determined at decadal time-scales[3–5], but it has not been possible to identify discrete events or to resolve deposition on near-annual timescales. Here we analyse ^{210}Pb activity profiles from sediment cores taken in the pristine Beni and Mamore river basins, which together comprise 720,000 km² of the Amazon basin, to investigate sediment accumulation patterns in the Andean–Amazonian foreland. We find that in most locations, sediment stratigraphy is dominated by discrete packages of sediments of uniform age, which are typically 20–80 cm thick, with system-wide recurrence intervals of about 8 yr, indicating relatively rare episodic deposition events. Ocean temperature and stream flow records link these episodic events to rapidly rising floods associated with La Niña events, which debouch extraordinary volumes of sediments from the Andes. We conclude that transient processes driven by the El

Niño/Southern Oscillation cycle control the formation of the Bolivian flood plains and modulate downstream delivery of sediments as well as associated carbon, nutrients and pollutants to the Amazon main stem.

Studies of modern flood-plain accumulation have described the spatial extent and depth of deposits[1,2], estimated flood-plain deposition using numerical models and surveys of grain size[6–9], or used a variety of mapping, field sampling and computations of the diffuse and channelized over-bank advection of turbid water[10]. Recent studies have measured flood-plain accumulation using geochronology sufficient to resolve these rates on decadal timescales[3–5,11]. However, no previous study has resolved the spatial and temporal distribution of individual accumulation events across large, dynamic fluvial dispersal systems. It is now possible to identify discrete events and measure the accumulation from such processes with near-annual resolution[12,13]. Our measurements along two rivers at a variety of distances from the channel reveal previously undocumented spatial and temporal patterns that reflect the hydraulics of sedimentation and the occurrence of flooding and sediment delivery forced by global atmospheric processes.

The Beni and Mamore rivers (Fig. 1) transport sediment from the rapidly eroding Bolivian Andes[14] across the flood plains of a large foreland basin[15,16]. Flood plains and channels are essentially pristine, without artificial levees, dams, dredging, roads, significant deforestation or cultivation, or other anthropogenic complications. The Beni drains 70,000 km^2 of the northern Bolivian Andes into the lowland Amazon basin and then through an additional 50,000 km^2 of forested flood plain, depositing approximately 100 Mt yr^{-1} of sediment as it traverses the foreland basin[13,17,18]. The adjacent Mamore drains a 600,000-km^2 basin. These basins are representative of the vast expanse of Andean–Amazonian foreland basins to the north.

Sampling was conducted at locations representing a variety of channel–flood-plain geometries, during August and September of 1999 and 2000 (ref. 13). A total of 276 sediment cores 65–160-cm deep were extracted (153 from Beni and 123 from Mamore) from surveyed transects at distances of 50–1,200 m from the channel, predominately from the higher, mature flood plain on the cut-bank side of the river. Such spatial coverage allows resolution of discrete deposition events across transects traversing hundreds of metres of flood plain, with cores typically spaced every 50 m, as well as measurement of sedimentation along thousands of kilometres of river.

Cores were X-rayed to evaluate sedimentary structures and potential post-deposition disturbance. After imaging, 115 of the cores (80 from Beni and 35 from Mamore) were cut, processed, and clay-normalized ^{210}Pb activity profiles were measured with methods described and calibrated elsewhere[12,19], which allow the identification of individual sediment packages and their dating with annual resolution. The CIRCAUS (constant initial reach clay activity, unknown sedimentation) procedure[12] for flood-plain geochronology accounts for the basin-wide variation in the ^{210}Pb activity of river-borne sediment and relies on only a few assumptions, each of which is testable.

More than 95% of the Beni and Mamore cores depict episodic sediment accumulation best described by the CIRCAUS model[12]. In most flood-plain locations, sediment arrives as discrete packages of uniform age across an observed depth range (Fig. 2). Granulometry and X-ray radiographs indicate that this sediment is silt-sized and is deposited as coherent packages in a low-energy environment. Fine horizontal laminations and other submillimetre-scale structures show that the flood-plain sediment has not been significantly disturbed since deposition and that bioturbation is negligible at most locations. Cross-bedding and other evidence for higher-energy deposition environments are rare on the cut-bank side of the flood plain, and are found mainly in point bar deposits close to the edge of the vegetation. Sediment packages are typically 20–80 cm thick, and vertical profiles from 6-m-high cut-bank outcrops indicate that the layers do not exceed 2 m in thickness. Hiatuses of decades occur between layers in cores with several events. Furthermore, the sediment at the flood-plain surface (after accounting for the meteoric cap) is often decades old, and in such cases is not blanketed by fresh sediment with higher ^{210}Pb activity from recent sedimentation events. Although Beni and Mamore flood-plain sediment arrives as discrete pulses, any particular flood-plain location receives sediment infrequently. Hence, episodic sedimentation is the predominant mechanism for flood-plain accumulation.

Averaged over these events, the accumulation rate varies with flood-plain distance from the active river channel (Fig. 3). High, variable rates proximal (<300 m) to the channel represent local processes that construct natural levees through frequent decanting of sediment over bank during annual floods—the few cores exhibiting constant sedimentation were located within this zone. Farther from the channel, lower, spatially uniform, temporally episodic rates reflect the extensive processes that convey most sediment onto the distal flood plain.

When accumulation dates from all cores are compiled (Fig. 4a), a basin-wide pattern emerges: distinct sedimentation pulses are

Figure 1 The Beni and Mamore river flood plains within the Llanos, northern Bolivia. The two rivers are the principal sediment and water sources for the Madeira River[17], the largest sediment source for the Amazon[10]. Elevations >300 m are depicted as grey shaded relief; lower elevations as a rainbow equal-area stretch. Flood-plain transects are denoted with squares whereas in-channel samples are denoted with crosses. Approximate location of the foredeep and forebulge were determined with GPS surveys of longitudinal river gradient. One-degree latitude is approximately 110 km.

separated by years to decades. This century-long geochronological record spans the entire foreland, suggesting that floods needed to facilitate widespread accumulation occur approximately every 8 yr (11 events in 90 yr). This is a separate phenomenon from the previous observation that many decades may pass between sedimentation events at a specific flood-plain location. Because younger events bury older ones and most of the cores are about 1-m deep, our record is biased towards recent events and densely sampled river reaches. Therefore, only the dates of the peak centres should be considered, not the relative heights.

To interpret this temporal pattern, we investigated climatic variability. Eastern Bolivia experiences high rainfall in the Andes during cold-phase El Niño/Southern Oscillation (ENSO) events (La Niña)[20], causing the Beni river to flood[21]. We used a sea temperature index (STI) appropriate for the Beni river (Fig. 4a). Over the last century, the nine La Niña years match the sediment accumulation record. Two

exceptions, 1983 and 1998, are minor cold-phase ENSO years that follow intense warm-phase ENSO years. Sediment accumulation correlates well with such transitional cold-phase years (1975 is non-transitional La Niña, and 1977 the only exception).

The Mamore flood plain spans a transitional region of climate response to ENSO[22], which seems to have migrated in the early 1970s: before 1970, rainfall was high during La Niña; after 1970, rainfall was lower during La Niña and higher or unaffected during El Niño[23]. However, the rainfall response in the Andean tributaries of the Mamore has remained the same; that is, elevated La Niña rainfall. After 1970, Mamore flood-plain runoff was no longer synchronous with Andean sources, thus affecting flooding hydrology. For locations spanning the Mamore foredeep, no sediment has accumulated since 1974. This suggests a hiatus in significant flooding following a change in rainfall response to ENSO.

To explore the mechanisms governing flood-plain accumulation, we examined water discharge at Rurrenabaque (Fig. 4b). Sediment accumulation consistently occurs whenever discharge rises more than $8,000 \, \mathrm{m^3 \, s^{-1}}$ over a few days. These rapid-rise years also correspond to peak discharges $>12,000 \, \mathrm{m^3 \, s^{-1}}$. However, there are four slow-rise years with maximum discharges above that threshold, although these events are not recorded in our cores. As a result, the record of maximum flooding does not correlate to La Niña as well as does our flood-plain accumulation record.

Beni flood-plain topographic surveys indicate that flood-plain inundation begins when discharges exceed $6,000 \, \mathrm{m^3 \, s^{-1}}$, a value exceeded annually[18]. However, distal flood plains do not exhibit chronic accumulation. Sedimentation is episodic in several specific ways: (1) events correspond only to large, rapid-rise floods; (2) neighbouring cores (within 1 km) typically record the same event, but there is little synchrony between locations tens of kilometres apart; and (3) at any specific location, sediment accumulates only during some floods, with a hiatus of decades typically separating sediment pulses 20–80 cm in thickness. The environment of deposition is low energy and silt rich. Suspended sediment in the Beni river is dominated by fine silts, whereas the bed is composed of sand[13,24], so source material for flood-plain sedimentation is derived from high in the water column. Inundation of the entire flood plain by sediment-laden water slowly decanted over levees during annual floods—the local mechanism that constructs the levees—would result in chronic, thin, synchronous sediment accumulation.

Instead, the thick episodic deposits are probably relatively small crevasse splays; delta-shaped deposits formed during levee failure. The banks are composed of loamy deposits susceptible to incision of
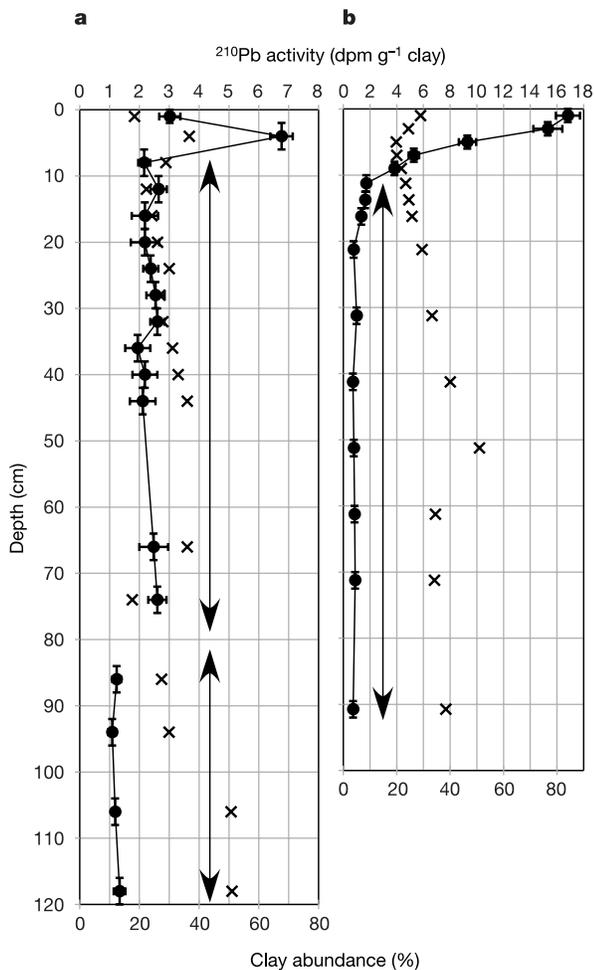
Figure 2 Unsupported ^{210}Pb activity profiles (circles) and clay abundance (crosses) from representative flood-plain cores. Accumulation events (denoted with vertical arrows) are dated with CIRCAUS geochronology[12,13]. Increases within the top 10 cm represent meteoric fallout. **a**, Beni river site located 2,000 m and 2,900 m from the channel when the sediment was deposited in 1974 (± 1.8 yr) and 1951 (± 1.9 yr). The meteoric cap is incomplete. X-radiographs depict fine laminations throughout the upper core, with minor cross-bedding below 80 cm depth. **b**, Mamore river site located 175 m from the river when sediment was deposited in 1944 (± 2.0 yr). The cap date is 1945. X-radiographs depict fine laminations throughout the core. These examples portray typical episodic accumulation events, without chronic sedimentation. Nearby sites along flood-plain transects record similar events, a characteristic result that suggests that such sediment packages blanket regions hundreds to thousands of metres in width and length. dpm, disintegrations per minute.
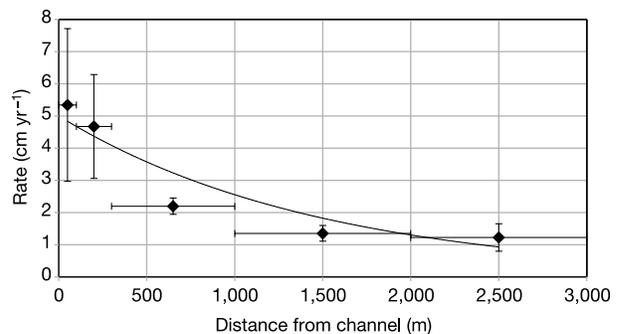
Figure 3 Spatial distribution of Beni flood-plain accumulation rates, averaged for five distance ranges, with best exponential fit ($r^2 = 0.82$). Because many flood-plain cores do not resolve the lower bound of accumulation events, rates are conservative. Owing to rapid channel migration across the flood plain, many of the core sites lay farther from the river during the most recent recorded deposition—concurrent river distances were measured from images (Landsat or aerial) bracketing the recorded date of each accumulation event. Projected across the flood plains of the Beni foreland basin[18], this relationship provides for an estimated average net sediment loss of about 100 Mt yr^{-1}.
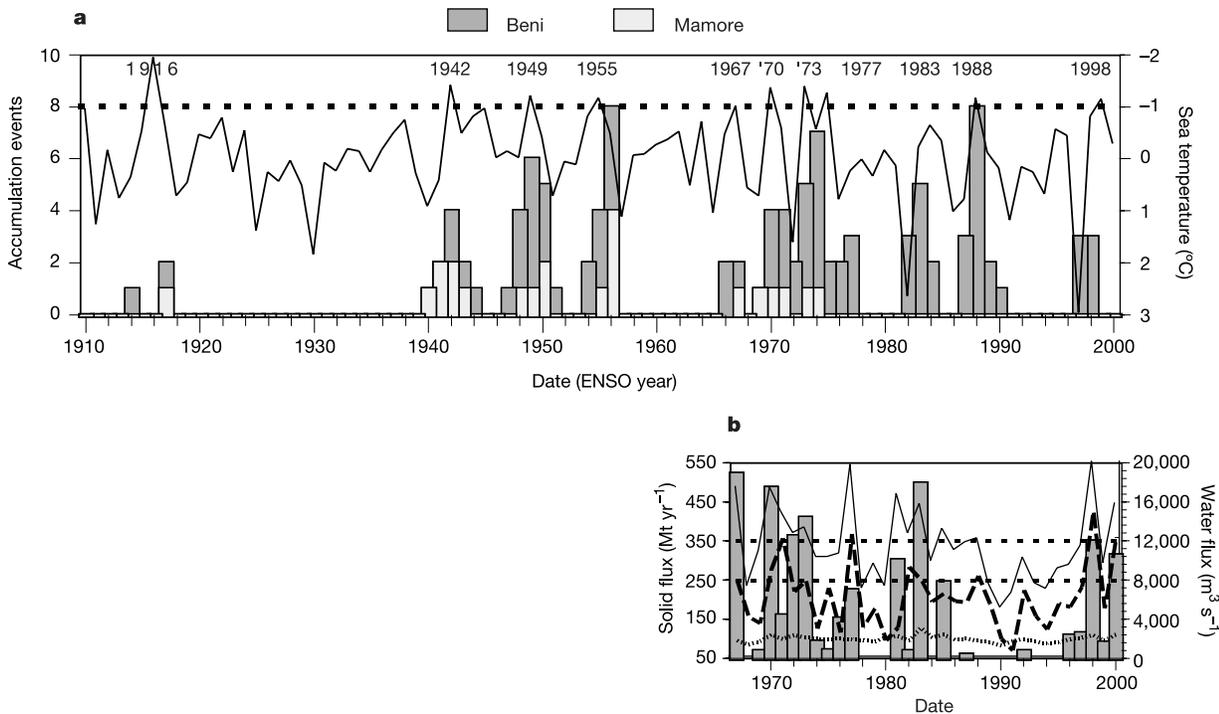
Figure 4 Temporal distribution of fluvial processes. **a**, Flood-plain accumulation events. STI is the average sea surface temperature anomaly in the eastern equatorial Pacific (150–80 W, 4 N–4 S) from November to February (the early rainy season months for Bolivia; temperatures are derived from a standard century-scale oceanographic record[30]). Marked years exhibit either STI < −1° (La Niña, threshold marked) or the flood-plain accumulation of sediment (CIRCAUS geochronology cannot discriminate events 1 yr apart). ENSO, sediment and water years run from October to September. **b**, Maximum (solid curve) and mean annual (dotted curve) water discharge, and rise to flood peak (dashed, 2–3-day increase in discharge) discharged from the Andes (Beni river at Rurrenabaque). The lower threshold shows both the minimum rapid flood rise (about 8,000 m^3 s^{-1}) associated with flood-plain accumulation and the mean annual sediment flux (about 250 Mt). The upper threshold represents the minimum discharge associated with flood-plain accumulation (approximately 12,000 m^3 s^{-1}). Also plotted is total sediment discharge (bars) conveyed by transitory bank-full floods (>6,000 m^3 s^{-1})[18], which comprise >60% of the average efflux—therefore, floods supply most of the sediment to the fluvial dispersal system and exceptional floods far surpass the mean annual flux and also account for much of the sediment exchanged due to channel migration[18].

crevasse channels during rapid overtopping[13]. Floodwater, decanted from high in the water column, would diverge into the densely vegetated flood plain, depositing an extensive lens of fine sediment within this low-energy environment. Such deposits are similar to short-lived crevasse splays described in the literature[2,25], including ancestral foredeep deposits preserved in the Andes[26]. Crevasse failure is more likely when the surrounding flood plain is relatively low, because of the higher hydraulic head or slope[27]. Conversely, a high flood plain is typically inundated by sediment-free water[28] from: (1) local rainfall and tributaries; (2) river water that enters the flood plain through distant crevasses but deposits its sediment as it traverses the inundated forest; and (3) water that slowly decants over bank, depositing its sediment as it crosses the vegetated levees. The prevalence of such 'black' water inhibits crevasse formation by reducing head. Hence, only a rapid-rise flood can engender the critical elevation differential between water in the channel and in the flood plain required to form crevasses.

Crevasse splays, triggered by large, rapid-rise ENSO floods, account for the preponderance of flood-plain sediment accumulation across the Bolivian Llanos (lowland plains), building stratigraphic sequences that are discontinuous in both time and space. Such critical floods also dominate sediment discharge from Andean tributaries across the foreland and into the large rivers of the Amazonian lowland (Fig. 4b), indicating considerable inter-annual variation of sediment supply and transport resulting from the interaction of Andean erosion and the dynamics of ENSO-driven climate. However, annual water discharge is relatively constant and previous studies have interpreted the fluxes along the Amazon main stem and the resulting sedimentation processes as following a regular annual cycle[10,29]. This implies an intervening region of active

sediment storage, exchange and geomorphic complexity. Because sediment supply, transport, deposition and exchange within these major Andean tributaries are orchestrated by extreme climate, such an 'alluvial capacitor' located between the foreland basins and the main-stem Amazon may further modulate particle transport to provide a more regular supply to Earth's largest river. □

1. Kesel, R. H., Yodis, E. G. & McCraw, D. J. An approximation of the sediment budget of the lower Mississippi River prior to major human modification. *Earth Surf. Process. Landforms* **17,** 711–722 (1992).
2. Aslan, A. & Autin, W. J. Evolution of the Holocene Mississippi River floodplain, Ferriday, Louisiana: insights of the origin of fine-grained floodplains. *J. Sedim. Res.* **69,** 800–815 (1999).
3. Nicholas, A. P. & Walling, D. E. Investigating spatial patterns of medium-term overbank sedimentation on floodplains: a combined numerical modeling and radiocaesium-based approach. *Geomorphology* **19,** 133–150 (1997).
4. He, Q. & Walling, D. E. Use of fallout Pb-210 measurements to investigate longer-term rates and patterns of overbank sediment deposition on the floodplains of lowland rivers. *Earth Surf. Process. Landforms* **21,** 141–154 (1996).
5. Goodbred, S. L. Jr & Kuehl, S. A. Floodplain processes in the Bengal Basin and the storage of Ganges-Brahmaputra river sediment: an accretion study using Cs-137 and Pb-210 geochronology. *Sediment. Geol.* **121,** 239–258 (1998).
6. Mertes, L. A. K. Rates of flood-plain sedimentation on the central Amazon River. *Geology* **22,** 171–174 (1994).
7. Howard, A. D. in *Lowland Floodplain Rivers: Geomorphological Perspectives* (eds Carling, P. A. & Petts, G. E.) (Wiley and Sons, Chichester, UK, 1992).
8. Pizzuto, J. E. Sediment diffusion during overbank flows. *Sedimentology* **34,** 301–317 (1987).
9. James, C. S. Sediment transfer to overbank sections. *J. Hydraul. Res.* **23,** 435–452 (1985).
10. Dunne, T., Mertes, L. A. K., Meade, R. H., Richey, J. E. & Forsberg, B. R. Exchanges of sediment between the floodplain and channel of the Amazon River in Brazil. *Geol. Soc. Am. Bull.* **110,** 450–467 (1998).
11. Allison, M. A., Kuehl, S. A., Martin, T. C. & Hassan, A. Importance of flood-plain sedimentation for river sediment budgets and terrigenous input to the oceans: Insights from the Brahmaputra-Jamuna River. *Geology* **26,** 175–178 (1998).
12. Aalto, R. & Nittrouer, C. A. Application of fallout ^{210}Pb geochronology to river-floodplain systems. *Sediment. Geol.* (submitted).
13. Aalto, R. *Geomorphic Form and Process of Mass Flux Within an Active Orogen: Denudation of the*

Bolivian Andes and Sediment Transport and Deposition Within the Channel-Floodplain Systems of the Amazonian Foreland. 365 Thesis, Univ. Washington (2002).

14. Aalto, R., Dunne, T. & Guyot, J. L. Geomorphic controls on Andean denudation rates. *J. Geol.* (in the press).

15. Horton, B. K. & DeCelles, P. G. The modern foreland basin system adjacent to the Central Andes. *Geology* **25**, 895–898 (1997).

16. Baby, P., Rochat, P., Mascle, G. & Hérail, G. Neogene shortening contribution to crustal thickening in the back arc of the Central Andes. *Geology* **25**, 883–886 (1997).

17. Guyot, J. L. *Hydrogéochimie des Fleuves de l'Amazonie Bolivienne*. Collection Études & Thèses (ORSTOM Ed.), Paris, (1993).

18. Aalto, R., Dunne, T., Maurice-Bourgoin, L., Guyot, J. L. & Nittrouer, C. A. Beni River morphology, migration, and sediment exchange between the river and its floodplain. *Geol. Soc. Am. Bull.* (submitted).

19. Nie, Y., Suayah, I. B., Benninger, L. K. & Alperin, M. J. Modeling detailed sedimentary 210-Pb and fallout 239–240-Pu profiles to allow episodic events: an application to Chesapeake Bay. *Limnol. Oceanogr.* **46**, 1425–1437 (2001).

20. Aceituno, P. On the functioning of the Southern Oscillation in the South America Sector Part I: Surface climate. *Mon. Weath. Rev.* **116**, 505–524 (1988).

21. Maurice-Bourgoin, L., Ronchail, J., Vauchel, P., Aalto, R. & Guyot, J. L. Climate controls (ENSO) on the flooding of the Beni River, a large Andean tributary of the Amazon. *EOS AGI Trans. Spring* A-09895 (2003).

22. Coelho, C. A. S., Uvo, C. B. & Ambrizzi, T. Exploring the impacts of the tropical Pacific SST on the precipitation patterns over South America during ENSO periods. *Theor. Appl. Climatol.* **71**, 185–197 (2002).

23. Ronchail, J. Variabilité pluviométrique en Bolivie lors des phases extrêmes de l'oscillation australe du Pacifique (1950–1993). *Bull. Inst. Fr. Etud. Andines* **27**, 687–698 (1998).

24. Guyot, J. L., Jouanneau, J. M. & Wasson, J. G. Characterisation of river bed and suspended sediments in the Rio Madeira drainage basin (Bolivian Amazonia). *J. Soc. Am. Earth Sci.* **12**, 401–410 (1999).

25. Smith, N. D., Cross, T. A., Dufficy, J. P. & Clough, S. R. Anatomy of an avulsion. *Sedimentology* **36**, 1–23 (1989).

26. Horton, B. K., Hampton, B. A. & Waanders, G. L. Paleogene synorogenic sedimentation in the Altiplano plateau and implications for initial mountain building in the central Andes. *Geol. Soc. Am. Bull.* **113**, 1387–1400 (2001).

27. Slingerland, R. L. & Smith, N. D. Necessary conditions for a meandering river avulsion. *Geology* **26**, 435–438 (1998).

28. Mertes, L. A. K. Description and significance of the perirheic zone on inundated floodplains. *Wat. Resour. Res.* **33**, 1749–1762 (1997).

29. Richey, J. E., Melack, J. M., Aufdenkampe, A. K., Ballester, V. M. & Hess, L. L. Outgassing from Amazonian rivers and wetlands as a large tropical source of atmospheric CO_2. *Nature* **416**, 617–620 (2002).

30. Meyers, S. D., Thelin, E. & O'Brien, J. J. Reconstruction of monthly SST in the tropical Pacific Ocean during 1868–1993 using adaptive climate basis functions. *Mon. Weath. Rev.* **127**, 1599–1612 (1999).

....

Boundary-layer mantle flow under the Dead Sea transform fault inferred from seismic anisotropy

Georg Rümpker[1,2], **Trond Ryberg**[1], **Günter Bock**[1] **& Desert Seismology Group**[*]

[1]*GeoForschungsZentrum Potsdam, Telegrafenberg, 14473 Potsdam, Germany*
[*] *A complete list of authors appears at the end of the paper*

....

Lithospheric-scale transform faults play an important role in the dynamics of global plate motion. Near-surface deformation fields for such faults are relatively well documented by satellite geodesy, strain measurements and earthquake source studies[1,2]**, and deeper crustal structure has been imaged by seismic profiling**[3]**. Relatively little is known, however, about deformation taking place in the subcrustal lithosphere—that is, the width and depth of the region associated with the deformation, the transition between deformed and undeformed lithosphere and the interaction between lithospheric and asthenospheric mantle flow at the plate boundary. Here we present evidence for a narrow, approximately 20-km-wide, subcrustal anisotropic zone of fault-parallel mineral alignment beneath the Dead Sea transform, obtained from an inversion of shear-wave splitting observations along a dense receiver profile. The geometry of this zone and the contrast between distinct anisotropic domains suggest subhorizontal mantle flow within a vertical boundary layer that extends through the entire lithosphere and accommodates the transform motion between the African and Arabian plates within this relatively narrow zone.**

At the southern end of the Dead Sea transform (DST), between the Dead Sea and the Red Sea, the Wadi Arava fault is the main active strike-slip fault[4–6] trending approximately N20E. Near the
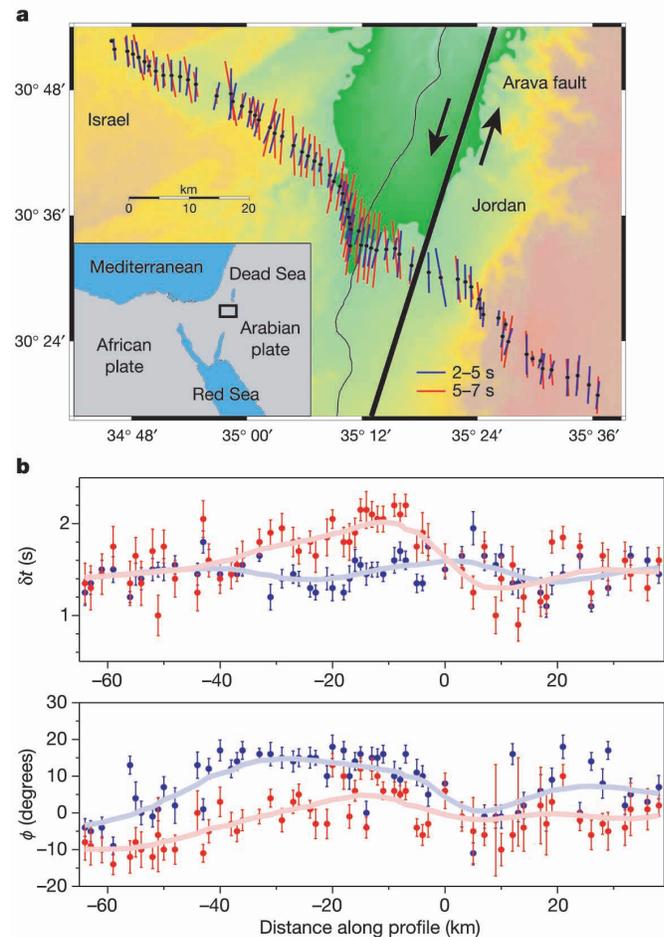
Figure 1 Study area and shear-wave splitting parameters. **a**, Map with topography and the locations of seismic stations for which the shear-wave splitting analysis was performed. The Arava fault (black line) strikes at approximately N20E. The bars indicate measured SKS splitting parameters for the period range of 2–5 s (blue) and 5–7 s (red). The orientation corresponds to the polarization direction of the fast shear wave (fast polarization ϕ) and the length is proportional to the delay time δt–1 s. **b**, Measured shear-wave splitting parameters (circles) along the profile (delay times and fast polarization directions) for the two period bands (2–5 and 5–7 s). The parameters are obtained by application of an inverse splitting operator to minimize the energy of the transverse SKS component[17]. A measure of error has been derived from the 95% confidence region as determined by the χ^2 distribution. For reasons of representation a factor of 0.4 is applied to the error scales used in this figure. The lines represent a smoothed version of the measurements, calculated by averaging the results within a sliding window.